

AMPLIFICATION OF SH WAVES BY AN ORTHOTROPIC BASIN

TAO ZHENG[†] AND MARIJAN DRAVINSKI^{*‡}

University of Southern California, Los Angeles, CA 90089-1453, U.S.A.

SUMMARY

Scattering of elastic waves by an orthotropic sedimentary basin is investigated for antiplane strain model using an indirect boundary integral equation approach. Both steady state and transient response were obtained for semicircular and semielliptical basins with different material properties. The results indicate that the basin geometry and the impedance contrast between the half-space and the basin have similar effects on the surface ground motion amplification as for the isotropic case. However, the material anisotropy may change significantly the fundamental resonant frequencies of the basin, resulting in different surface displacement amplification patterns. In addition, it was observed that the arrival time of the main disturbance on the surface strongly depends on material anisotropy for different angles of incidence. The results demonstrate that material anisotropy may be very important in explaining surface ground motion amplification for sedimentary basins. © 1998 John Wiley & Sons, Ltd.

Earthquake Engng. Struct. Dyn., **27**, 243–257 (1998)

KEY WORDS: anisotropic basin; site response

INTRODUCTION

Scattering of elastic waves by isotropic subsurface inclusions has been the subject of many studies in non-destructive evaluation of materials and prediction of earthquake-induced ground motion atop a sediment-filled basin.^{1,2} However, increasing use of composite materials in engineering design and the need to investigate the fine details of the Earth's structure necessitate the research on the scattering of elastic waves by irregularities in anisotropic media. For example, displacement solution due to a surface pulse in a composite medium with defects can be used to compute the acoustic material signature.³ Similarly, geophysical studies have found that seismic anisotropy is a wide-spread phenomenon in Earth rocks with a variety of mechanisms which give rise to anisotropy.^{4,5}

Two- and three-dimensional scattering of elastic waves by an isotropic alluvial valley were studied by a number of researchers. An extensive literature review can be found in the paper by Bouchon and Coutant.² These studies provide reasonable understanding of the physical basis of the site-amplification problems.

For anisotropic media studies, detailed survey of literature can be found in Nayfeh.⁶ As for scattering of elastic wave problems Rajapakse and Gross³ examined the response of an orthotropic elastic medium with an embedded cavity of arbitrary shape due to transient pressurization using a boundary integral equation method. Karabulut and Ferguson⁷ studied SH-wave propagation in transversely isotropic medium by using discrete wave number boundary integral method. Two semiinfinite half-spaces and a multilayered earth model were considered.

* Correspondence to: M. Dravinski, Department of Mechanical Engineering, Olin Hall 430, University of Southern California, Los Angeles, CA 90089-1453, U.S.A. E-mail: mdravins@mizar.usc.edu

[†] Graduate Student

[‡] Professor

Contract grant sponsor: All University Predoctoral Merit Fellowship

In this paper, scattering of SH-waves by a sedimentary basin of arbitrary shape embedded in a half-space is investigated for orthotropic materials. The solution is derived by using an indirect boundary integral equation approach. Numerical results are obtained for semicircular and semielliptical basins with different material properties. The steady-state displacement field is calculated for different angles of incidence and the transient response is obtained through the Fourier synthesis. The role of material anisotropy, impedance contrast, incident field, and the basin geometry on the surface response is discussed in detail.

STATEMENT OF PROBLEM

Geometry of the problem is depicted in Figure 1. The problem consists of a half-space with a sedimentary basin of arbitrary shape. The domains of the half-space and the basin are denoted by D_1 and D_2 , respectively. The interface C between the basin and the half-space is assumed to be sufficiently smooth. Material is assumed to be linearly elastic, homogeneous and orthotropic with the symmetry planes coincident with the Cartesian co-ordinate system (x_1, x_2, x_3) .

For an orthotropic material and antiplane strain model, u_2 is the only non-zero displacement component describing horizontally polarized SH motion. Using unabridged notation (u, v, w) and (x, y, z) instead of (u_1, u_2, u_3) and (x_1, x_2, x_3) , respectively, the equation of motion for the antiplane strain model becomes (Reference 6, pp. 26–29)

$$C_{66}^{(j)} \frac{\partial^2 v_j}{\partial x^2} + C_{44}^{(j)} \frac{\partial^2 v_j}{\partial z^2} = \rho^{(j)} \frac{\partial^2 v_j}{\partial t^2}, \quad j = 1, 2 \quad (1)$$

Here, j represents the domain D_j . The stress field is specified by⁶

$$\sigma_{xy}^{(j)} = C_{66}^{(j)} \frac{\partial v_j}{\partial x}, \quad j = 1, 2 \quad (2)$$

$$\sigma_{yz}^{(j)} = C_{44}^{(j)} \frac{\partial v_j}{\partial z}, \quad j = 1, 2 \quad (3)$$

The stress-free boundary conditions along the surface $z = 0$ can be written as

$$\sigma_{yz}^{(j)} = 0, \quad z = 0, \quad \mathbf{x} \in D_j, \quad j = 1, 2 \quad (4)$$

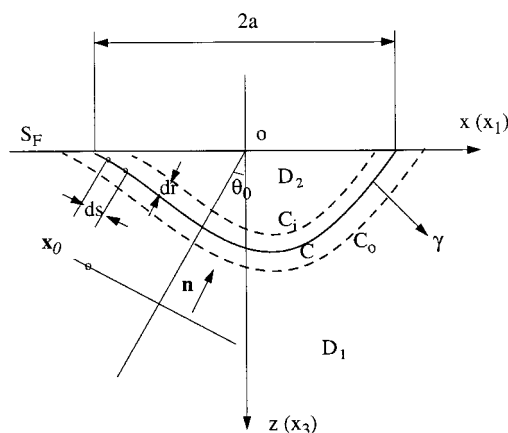


Figure 1. Problem geometry. C : basin-half-space interface with unit normal γ and surface width $2a$; C_i, C_o : inner and outer auxiliary surfaces; dr : separation between the interface C and the auxiliary surfaces; \mathbf{n} and θ_0 : the direction of propagation and the angle of incidence; \mathbf{x}_0 : reference point; ds : separation between the collocation points; D_1 and D_2 domains of the half-space and the basin, respectively

Continuity of displacement and traction field along the interface C as required to ensure the perfect bonding between the basin and the half-space can be stated as

$$\begin{cases} v_1(\mathbf{x}, t) = v_2(\mathbf{x}, t), & \mathbf{x} \in C \\ t_y^{(1)}(\mathbf{x}, t) = t_y^{(2)}(\mathbf{x}, t), & \mathbf{x} \in C \end{cases} \quad (5)$$

where $t_y^{(j)}$ ($j = 1, 2$) represents the y -component of traction vector which is determined by

$$t_y = C_{66} \frac{\partial v}{\partial x} \gamma_x + C_{44} \frac{\partial v}{\partial z} \gamma_z \quad (6)$$

Here, γ is the outward unit normal on the interface C (see Figure 1).

For the steady-state solution, the incident SH-wave is assumed to be of the form⁶

$$v^{\text{inc}} = \exp\{i(\zeta x \sin \theta_0 - \zeta z \cos \theta_0 - \omega t)\} \quad (7)$$

where θ_0 is the angle of incidence, ω is the circular frequency, $\zeta (= \omega/\beta_1)$ denotes the shear wave number, and β_1 represents the shear wave velocity in the half-space.

This concludes the statement of the problem. The solution of the problem is presented next.

SOLUTION OF PROBLEM

Steady-state solution

As the incident wave strikes the interface C , it is partially transmitted into the basin and partially reflected back into the half-space. Consequently, the waves in the half-space consist of the free- and scattered-wave fields, while the waves inside the basin comprise of the scattered-wave field only. The displacement components in the half-space and the basin can be expressed as

$$\begin{cases} v_1 = v^{\text{ff}} + v_1^{\text{s}}, & \mathbf{x} \in D_1 \\ v_2 = v_2^{\text{s}}, & \mathbf{x} \in D_2 \end{cases} \quad (8)$$

where the superscripts s and ff denote the scattered and free field, respectively.

Free field

A plane wave solution to the equation of motion, equation (1), can be of the form

$$v = V \exp\{i(\zeta \mathbf{n} \cdot \mathbf{x} - \omega t)\} \quad (9)$$

where $\zeta = \omega/\beta$ represents the wave number, \mathbf{n} is unit vector along the propagation direction and ω is the circular frequency. Substituting equation (9) into the equation of motion, equation (1), together with the requirement of non-zero amplitude V , leads to the following expression for SH-wave velocity

$$\beta = \sqrt{\frac{C_{66}n_x^2 + C_{44}n_z^2}{\rho}} \quad (10)$$

Equation (10) shows that the wave velocity depends not only on material properties, but also on the propagating direction. If the material is isotropic, i.e. $C_{44} = C_{66} = \mu$, equation (10) turns out to be the familiar one: $\beta = \sqrt{\mu/\rho}$, where μ denotes the shear modulus.

It is easy to show that for an incident SH-wave propagating in the direction $\mathbf{n}^{\text{inc}} = (\sin \theta_0, 0, -\cos \theta_0)$ and of the form

$$v^{\text{inc}} = \exp\{i(\zeta x \sin \theta_0 - \zeta z \cos \theta_0 - \omega t)\} \quad (11)$$

the corresponding free field is given by

$$v^{\text{ff}} = 2 \exp(i\zeta x \sin \theta_0) \cos(\zeta z \cos \theta_0) \exp(-i\omega t) \quad (12)$$

Here θ_0 denotes the angle of incidence.

Scattered-wave field

Assuming that the scattered-wave field can be expressed in terms of single-layer potentials^{8–10} then it follows that

$$v_1^s(\mathbf{r}) = \int_{C_i} q_1(\mathbf{r}_i) G_1(\mathbf{r}, \mathbf{r}_i) d\mathbf{r}_i, \quad \mathbf{r} \in D_1, \quad \mathbf{r}_i \in C_i \quad (13)$$

$$v_2^s(\mathbf{r}) = \int_{C_o} q_2(\mathbf{r}_o) G_2(\mathbf{r}, \mathbf{r}_o) d\mathbf{r}_o, \quad \mathbf{r} \in D_2, \quad \mathbf{r}_o \in C_o \quad (14)$$

where C_i , and C_o are the auxiliary surfaces defined inside and outside the basin, respectively, q_1 , q_2 are the unknown density functions, and G_1 , G_2 are the Greens functions associated with a line load in a half-space.

Assuming that the density functions q_1 , q_2 represent system of discrete point sources along the auxiliary surfaces C_i and C_o , respectively, it follows that

$$q_1(\mathbf{r}_i) = \sum_{m=1}^M a_m \delta(|\mathbf{r}_i - \mathbf{r}_m|), \quad \mathbf{r}_m \in C_i \quad (15)$$

$$q_2(\mathbf{r}_o) = \sum_{l=1}^L b_l \delta(|\mathbf{r}_o - \mathbf{r}_l|), \quad \mathbf{r}_l \in C_o \quad (16)$$

Here, a_m , b_l represent the unknown source intensities and M , L are the orders of approximation along C_i and C_o , respectively. Substitution of equations (15) and (16) into equations (13) and (14) results in the scattered-wave field

$$v_1^s(\mathbf{r}) = \sum_{m=1}^M a_m G_1(\mathbf{r}, \mathbf{r}_m), \quad \mathbf{r}_m \in C_i \quad (17)$$

$$v_2^s(\mathbf{r}) = \sum_{l=1}^L b_l G_2(\mathbf{r}, \mathbf{r}_l), \quad \mathbf{r}_l \in C_o \quad (18)$$

The Greens functions in this problem are

$$G_j(\mathbf{r}, \mathbf{r}_o) = \frac{i}{4} [H_0^{(1)}(k_j \sigma_1^{(j)}) + H_0^{(1)}(k_j \sigma_2^{(j)})], \quad j = 1, 2 \quad (19)$$

where $H_0^{(1)}(\cdot)$ denotes Hankel function of the first kind and of order zero, and

$$\sigma_1^{(j)} = \sqrt{\left(\frac{x - x_0}{\alpha^{(j)}}\right)^2 + (z - z_0)^2}$$

$$\sigma_2^{(j)} = \sqrt{\left(\frac{x - x_0}{\alpha^{(j)}}\right)^2 + (z + z_0)^2}$$

$$\alpha^{(j)} = \sqrt{\frac{C_{66}^{(j)}}{C_{44}^{(j)}}}$$

$$k_j = \omega \sqrt{\frac{\rho_j}{C_{44}^{(j)}}}$$

$$\mathbf{r}_0 = (x_0/\alpha, 0, z_0)$$

Source densities

The free field and the scattered-wave field satisfy both the equation of motion, equation (1), and the stress-free boundary condition, equation (4). Therefore, the only conditions that need to be imposed are the continuity conditions, equation (5). Substituting equation (8) into equation (5) yields the following results:

$$\sum_{m=1}^M a_m G_1(\mathbf{r}, \mathbf{r}_m) - \sum_{l=1}^L b_l G_2(\mathbf{r}, \mathbf{r}_l) = -v^{\text{ff}}(\mathbf{r}) \quad (20)$$

$$\sum_{m=1}^M a_m G_{1n}(\mathbf{r}, \mathbf{r}_m) - \sum_{l=1}^L b_l G_{2n}(\mathbf{r}, \mathbf{r}_l) = -v_n^{\text{ff}}(\mathbf{r}) \quad (21)$$

where $G_{1n}(\cdot)$, $G_{2n}(\cdot)$, and v_n^{ff} are known.

Choosing N observation points, $\mathbf{r} = \mathbf{r}_i$, $i = 1, 2, \dots, N$ along the interface C , equations (20) and (21) can be written as

$$\mathbf{A}\mathbf{a} = \mathbf{f} \quad (22)$$

where matrix \mathbf{A} , of order $2N \times (M + L)$, and vector \mathbf{f} , of order $2N \times 1$, are known and vector $\mathbf{a} = [a_1, \dots, a_M, b_1, \dots, b_L]^T$ contains the unknown source intensities. Equation (22) is solved in the least-squares sense using the QR-decomposition.¹¹

NUMERICAL RESULTS

This section includes convergence analysis, steady-state results, resonance discussion and transient response. In the convergence analysis, the accuracy of the proposed method is investigated and the optimum parameters for each model are determined. Using the optimized parameters, the surface displacements are computed for a plane harmonic incident SH-wave. Resonant frequencies of the models are studied with the help of the spectral search method. The transient response is obtained through the FFT technique. The numerical results for different models are compared and the role of anisotropy on the surface response is discussed as well.

Table I. Model parameters

Model	A (isotropic)	B	B1	C
$C_{44}^{(1)}$	6	6	6	12.5
$C_{66}^{(1)}$	6	12	12	25
ρ_1	1.5	1.5	1.5	2
$C_{44}^{(2)}$	1	1	1	1
$C_{66}^{(2)}$	1	2	2	2
ρ_2	1	1	1	1
β_1^h/β_1^v	1	1.41	1.41	1.41
β_1^h/β_2^h	2	2	2	2.5
β_1^v/β_2^v	2	2	2	2.5
ρ_1/ρ_2	1.5	1.5	1.5	2
$I_{1,2}$	3	3	3	5
Geometry	semicircular	semicircular	semielliptic	semicircular
Principal axes	$R_1 = R_2 = 1$	$R_1 = R_2 = 1$	$R_1 = 1; R_2 = 0.7$	$R_1 = R_2 = 1$

Models

In order to analyze the role of material anisotropy, the basin geometry and the impedance contrast on the surface response, four different models are considered. Models A, B and C incorporate semicircular basin, while model B1 consists of a semielliptical basin. Materials in model A are isotropic, and those in models B, B1 and C are orthotropic. Throughout, the half-width, density and material constant $C_{44}^{(2)}$ of the basin are normalized to unity. Isotropy factor⁷ is defined as the ratio between the horizontal and the vertical SH-wave velocity. For an orthotropic material, the isotropy factor is

$$\frac{\beta^h}{\beta^v} = \sqrt{\frac{C_{66}}{C_{44}}} \quad (23)$$

where β^h and β^v denote the horizontal and vertical SH-wave velocity, respectively.

The impedance contrast $I_{1,2}$ and the dimensionless frequency η are defined as¹⁷

$$I_{1,2} = \frac{\rho_1 \beta_1}{\rho_2 \beta_2} \quad (24)$$

$$\eta = \frac{2a}{\lambda_{\text{inc}}} = \frac{\omega}{\pi \beta_1} \quad (25)$$

where $2a$ represents the width of the basin on the surface S_F (Figure 1) and λ_{inc} denotes the incident wavelength ($\lambda_{\text{inc}} = (2\pi/\omega)\beta_1$). The parameters of the models are listed in Table I.

Model A consists of an isotropic semicircular basin for which there is an exact solution available.¹⁶ Model B incorporates a semicircular anisotropic basin while model C consists of an anisotropic circular basin with impedance contrast higher than in the case of model B ($I_{1,2}^C = 5$ compared to $I_{1,2}^B = 3$). Model B1 consists of a semielliptical anisotropic basin. These models will allow us to investigate the role of anisotropy, impedance contrast, and geometry upon surface ground motion.

Convergence analysis

The indirect boundary integral equation method requires the following parameters (Figure 1): N —number of collocation points along the interface C between the half-space and the basin, M, L —number of source points along the auxiliary surfaces C_i and C_o , respectively, and dr —spacing between the auxiliary surfaces C_i , C_o and the interface C .

The following relationships were suggested by Ding and Dravinski:¹²

$$ds < \frac{1}{10} \lambda^{\text{inc}} \quad (26)$$

$$dr \simeq 3 ds \quad (27)$$

$$\frac{2N}{M+L} = 2.25 \sim 4.0 \quad (28)$$

$$M = L \quad (29)$$

where ds denotes the spacing between two adjacent collocation points and λ^{inc} is the incident wavelength.

The basin interface C is specified by

$$\begin{cases} x = R_1 \cos \theta, \\ z = R_2 \sin \theta, \quad 0 \leq \theta \leq \pi \end{cases} \quad (30)$$

where the principle axes R_1 and R_2 are given in Table I.

The inner and outer sources are placed along the surfaces C_i and C_o , respectively, defined by

$$C_i: \begin{cases} x = R_{1i} \cos \theta, \\ z = R_{2i} \sin \theta, \quad 0 \leq \theta \leq \pi \end{cases} \quad (31)$$

$$C_o: \begin{cases} x = R_{1o} \cos \theta, \\ z = R_{2o} \sin \theta, \quad 0 \leq \theta \leq \pi \end{cases} \quad (32)$$

with the principal axes being defined by

$$\begin{cases} R_{1,2i} = \xi_i R_{1,2}, \\ R_{1,2o} = \xi_o R_{1,2}, \quad 0 < \xi_i < 1; \quad 1 < \xi_o; \end{cases} \quad (33)$$

Here the parameters ξ_i and ξ_o are determined according to equations (26)–(29).

Therefore, if the incident wavelength is given, then ds can be chosen according to equation (26) and all other parameters can be determined in accordance with relations (27)–(29). Since the spacing ds depends on the number of collocation points N , the key problem is to determine N .

To establish the best number of collocation points N , the following convergence error is proposed:

$$\text{Er} = \frac{\sum_{i=1}^{N_s} (|v_s^n(\mathbf{r}_i)| - |v_s^{n-1}(\mathbf{r}_i)|)^2}{\sum_{i=1}^{N_s} (|v_s^n(\mathbf{r}_i)|)^2}, \quad \mathbf{r}_i \in S_F \quad (34)$$

Here, N_s is the number of observation points on the surface S_F (Figure 1), and the superscripts n and $n-1$ represent two consecutive iterations for the surface response. The subscript s denotes the surface displacement. As the numerical calculations converge at each observation point, the error Er should approach zero. In practice, the minimum error or the error less than a certain tolerance is being sought.

Throughout the analysis, the number of observation points N_s used to compute the error Er is chosen to be 501. The observation points are equally spaced over the range of $x \in [-2, 2]$, and the ratio of $2N/(M+L)$ is chosen to be 2.5.

It is important to determine the relationship between the error Er and the number of collocation points N for different frequencies and angles of incidence. Figure 2 displays these results for model *B*. Similar calculations were performed for all other models and the results for the minimum number of collocation points for the error $\text{Er} < 0.01$ are listed in Table II.

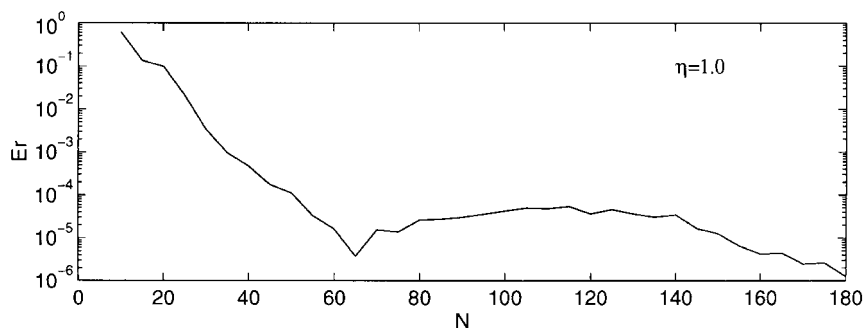


Figure 2. The relative error E_r as a function of the number of collocation points N along interface C for model B (vertical incidence). $\theta_0 = 0$, $\eta = 1$, $dr = 3$ ds, $M = L$, $2N/(M + L) = 2.5$, $x \in [-2, 2]$, $N_s = 501$

Table II. Minimum number of collocation points N for E_r less than 0.01

Incidence θ_0	Frequency η	Model A	Model B	Model B1	Model C
0°	1	50	30	25	85
0°	2	85	35	40	110
90°	1	50	35	45	75
90°	2	85	75	70	115

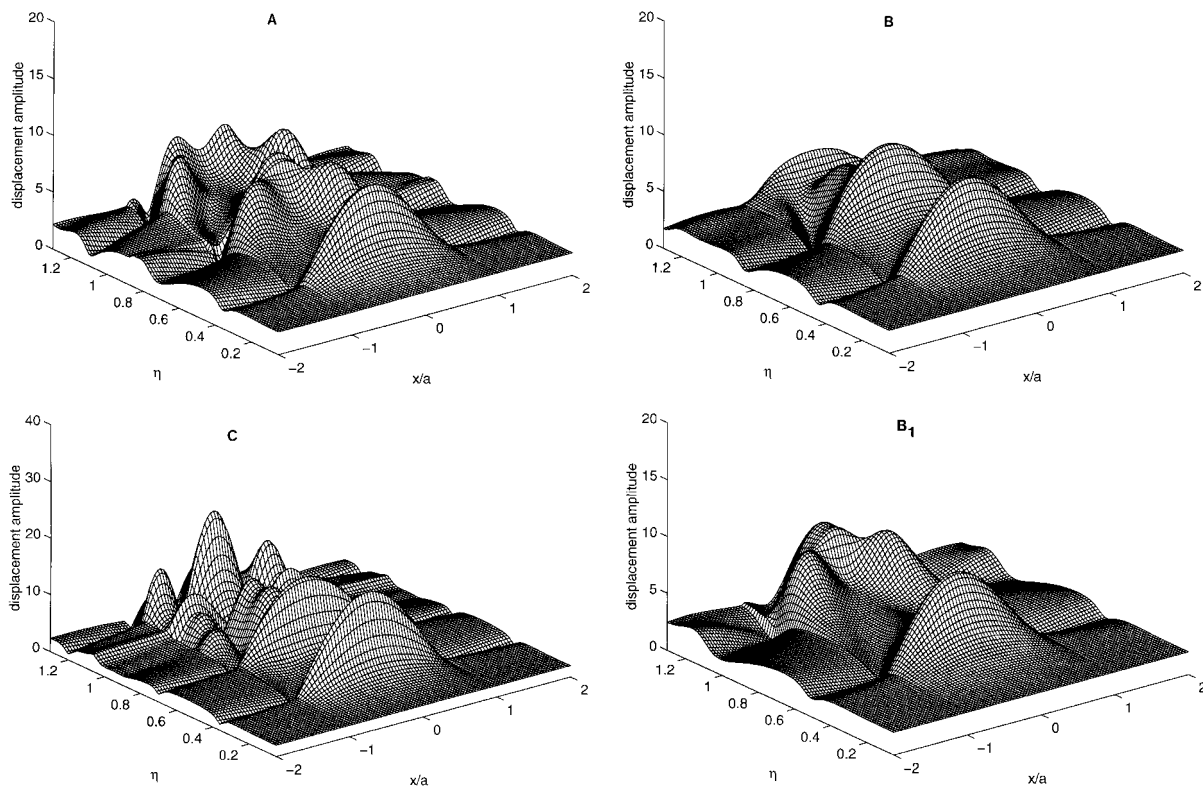


Figure 3. Surface displacement spectral amplitude for four models (Model A: top left; Model B: top right, Model C: bottom left, and Model B1: bottom right) as a function of space (x/a ; $a = R_1$) and dimensionless frequency (η) for a vertical incident SH-wave

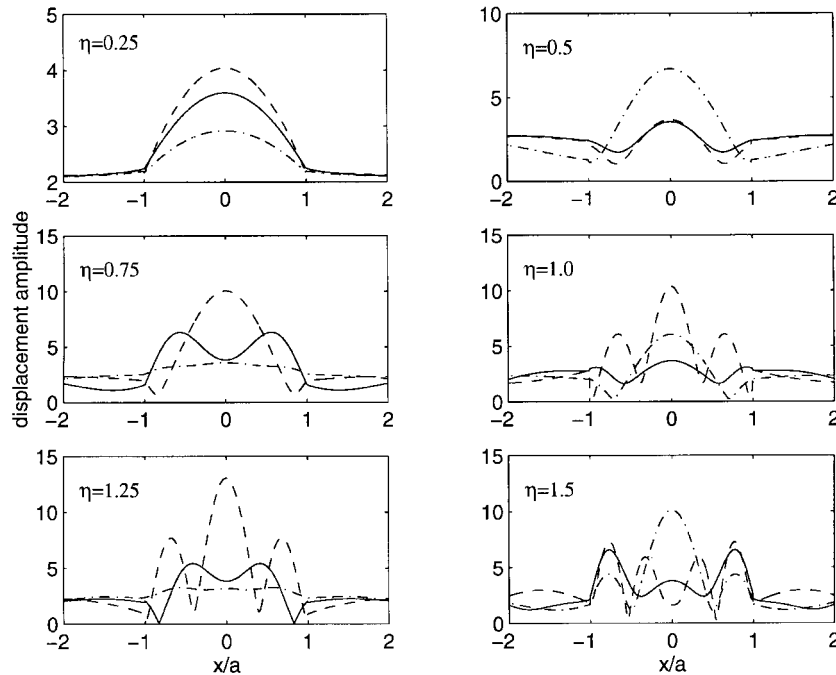


Figure 4. Comparison of surface displacement spectral amplitude for semicircular models for six different frequencies η and a vertical incident SH-wave. Models: A (isotropic: solid line), B (orthotropic: dash-dot line), and C (orthotropic with larger impedance contrast: dash line)

It can be seen from Table II that the minimum number of collocation points increases with increase in the frequency and the angle of incidence.

In order to test the accuracy of the proposed method, the transparency test was performed next. In this test, the material properties of the basin and the half-space are assumed to be the same. Consequently, there should be no scattering effects in the basin and in the half-space. It was found that indeed the surface displacement amplitude approaches to the value of the free field. For the sake of reducing the number of figures, the transparency results are omitted.

Now that the minimum number of collocation points N was obtained for each model, all other parameters necessary for numerical calculations can be determined by the empirical relations given by equations (27)–(29).

This concludes the convergence analysis of the problem. The steady-state results are considered next.

Steady-state response

For a vertical incidence, the surface displacement spectral amplitude as a function of frequency and location for the four models is shown by Figure 3. The following conclusions can be made about the steady-state results:

1. Presence of sedimentary basin changes significantly the surface ground motion.
2. For the same input and basin geometry, isotropic and anisotropic basins may produce significantly different surface motion (compare models A and B).
3. For anisotropic basins, surface motion strongly depends on the impedance contrast between the sediment and the bedrock (compare models B and C).
4. Shape of anisotropic basin is important in surface motion amplification (compare models B and B1).

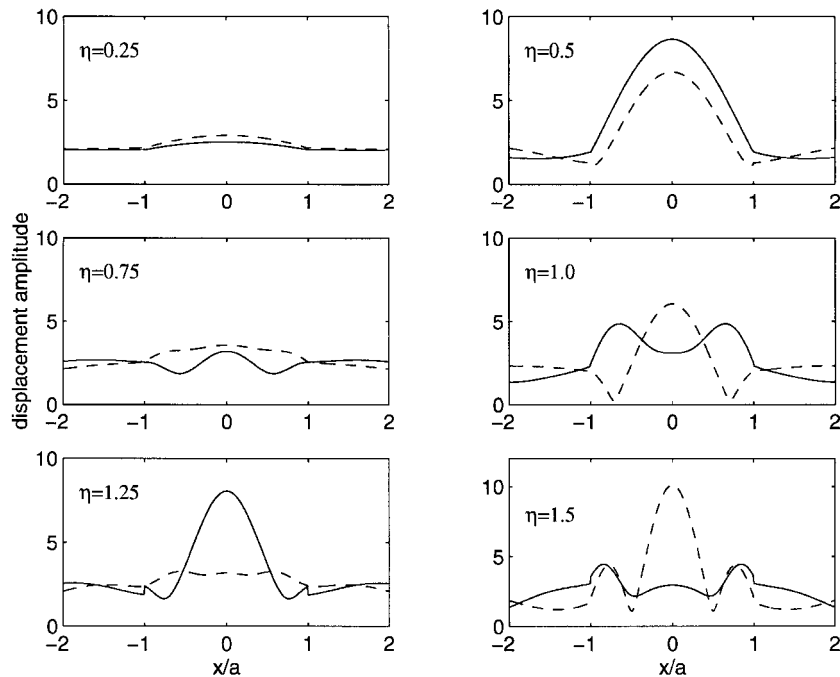


Figure 5. Comparison of surface displacement spectral amplitude for a semicircular and a semielliptical orthotropic basins at six different frequencies η and a vertical incidence. Models: B (semicircular: solid line) and B1 (semielliptical: dash line)

Although not presented here, surface ground motion is found to be very sensitive upon the angle of incidence as well.

More precise illustration of the differences between the surface response of semicircular basins (models A, B, and C) can be seen in Figure 4. Here, surface spectral amplitude is shown for an isotropic and two orthotropic models. It is obvious that anisotropy plays a major role in the surface ground motion amplification. The motion is also very sensitive upon the location of the observation station and the frequency of incident wave.

The role of the basin geometry in response of an anisotropic basin can be seen in more detail from the results of Figure 5 which depicts surface displacement spectral amplitude for a semicircular (B) and a semielliptical (B1) models. These results clearly display that in addition to the frequency and station location, surface ground motion amplification is very sensitive upon the basin geometry.

Resonance analysis

Resonance phenomenon is important in estimating earthquake-induced ground motion on the surface of a sedimentary basin.^{13,17} Resonant frequencies are defined as the frequencies at which the peak surface displacement amplitude reaches maximum.¹⁷ This idea is extended now to the anisotropic basin considered earlier and the resonant frequencies are identified using the spectral search method. It should be noted that the resonance analysis is done in the frequency domain ω . Use of dimensionless frequency η would introduce the dependance upon the angle of incidence.

For different angles of incidence, the peak displacement amplitude spectra for the four models are shown in Figure 6. The resonant frequencies can be clearly identified for all models. The analysis will focus only

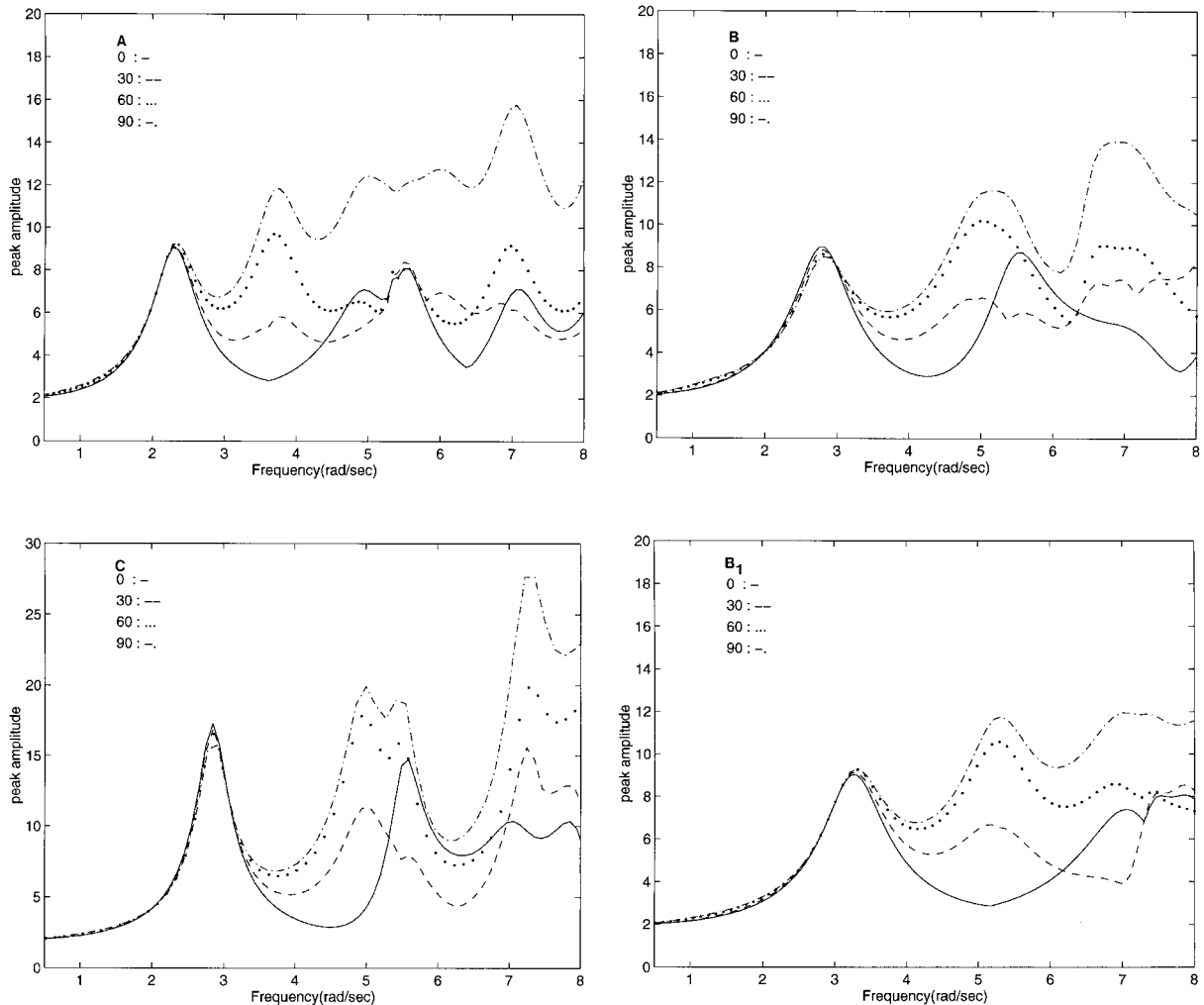


Figure 6. Peak surface displacement spectral amplitude for the four models (Model A: top left; Model B: top right, Model C: bottom left, and Model B1: bottom right) and different angles of incidence: $\theta_0 = 0^\circ$ (solid); $\theta_0 = 30^\circ$ (dash); $\theta_0 = 60^\circ$ (dot); $\theta_0 = 90^\circ$, (dash-dot)

on the fundamental frequency which is listed in Table III. Based on these results, the following conclusions can be made about the fundamental frequency of anisotropic basins:

1. For the same geometry, the fundamental frequency of anisotropic basin is different from that corresponding to an isotropic one ($\omega_1^B \neq \omega_1^A$);
2. The fundamental frequency is independent of the impedance contrast ($\omega_1^B = \omega_1^C$);
3. The fundamental frequency is strongly sensitive to the basin geometry ($\omega_1^{B1} \neq \omega_1^B$); and
4. The fundamental frequency is independent of the angle of incidence.

Property 1 ($\omega_1^B > \omega_1^A$ for the choice of models A and B) can be explained as an increase in the overall stiffness of the basin. Namely, for an isotropic case (model A), elastic constant $C_{44} = C_{66} = \mu$, while for an orthotropic case (model B), $C_{66} > C_{44}$. It should be noted that although fundamental frequency is independent of the impedance contrast (property 2), the corresponding surface motion amplification is not. Sensitivity of

Table III. The fundamental frequency for each model

Model	A	B	C	B1
ω_1 (s^{-1})	2.34	2.83	2.83	3.31

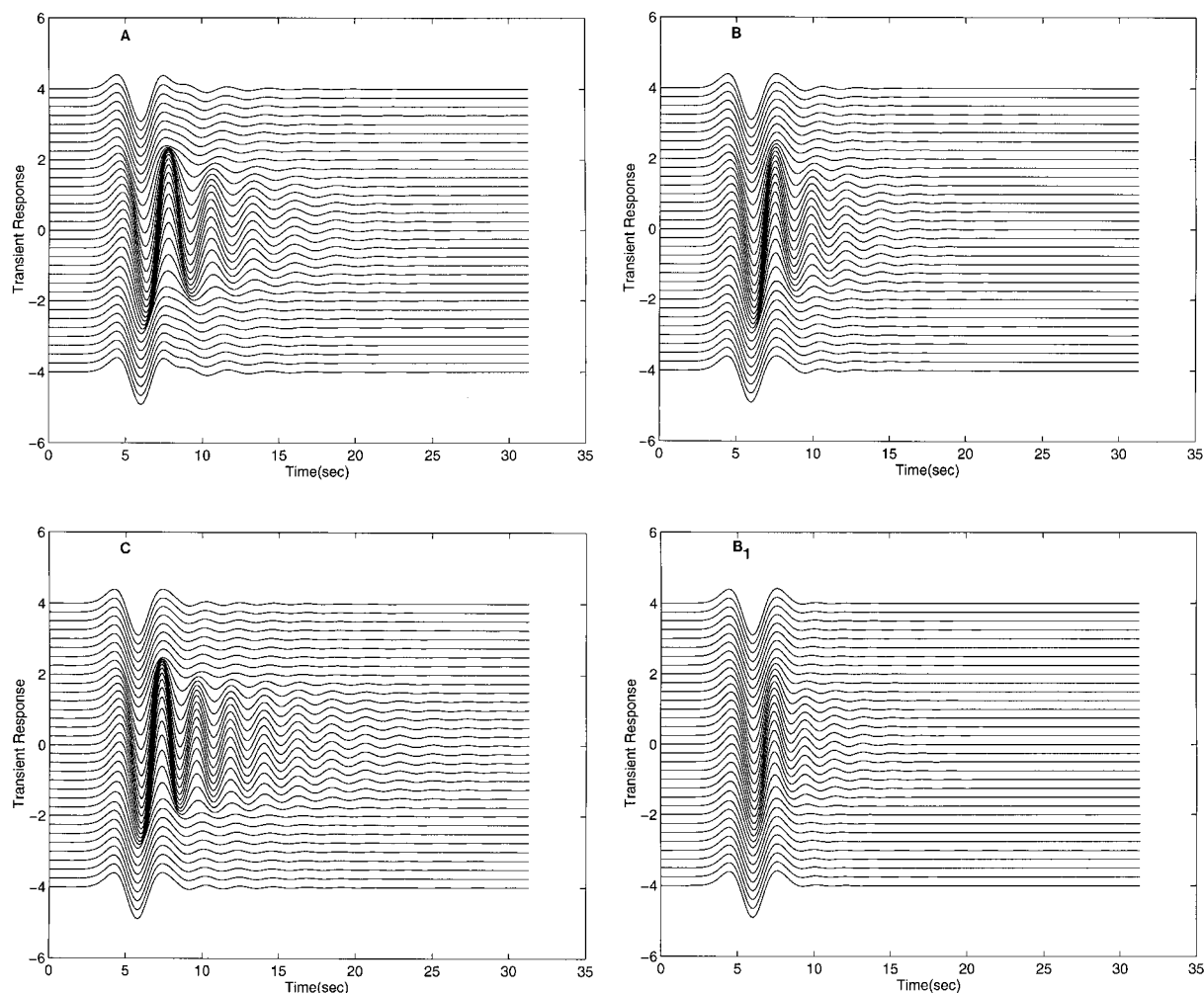


Figure 7. Transient surface response $v(x, 0, t)$ for four models (Model A: top left; Model B: top right, Model C: bottom left, and Model B1: bottom right) and a vertical incident Ricker wavelet with $t_p = 4$ s and $t_s = 5$ s. Thirty-three equally spaced points span the range $x \in [-2, 2]$. The wavefront at $t = 0$ is the plane passing through the point $(x_0, y_0, z_0) = (0, 0, 2)$. $N = 110, M = L = 44$. The FFT parameters: $\Delta\omega = 0.2$ rad/s; $\Delta t = 0.12272$; $n = 256$. (Note, the scale for the vertical axis corresponds to the displacement spectral amplitude.)

the fundamental frequency upon the basin geometry can be explained as a change in overall stiffness of the basin as geometry changes resulting in different resonant frequencies. It should be noted that the properties 2–4 were identified to hold for fundamental frequency of isotropic basins as well.¹⁷

This concludes resonance analysis of the problem. Transient results are considered next.

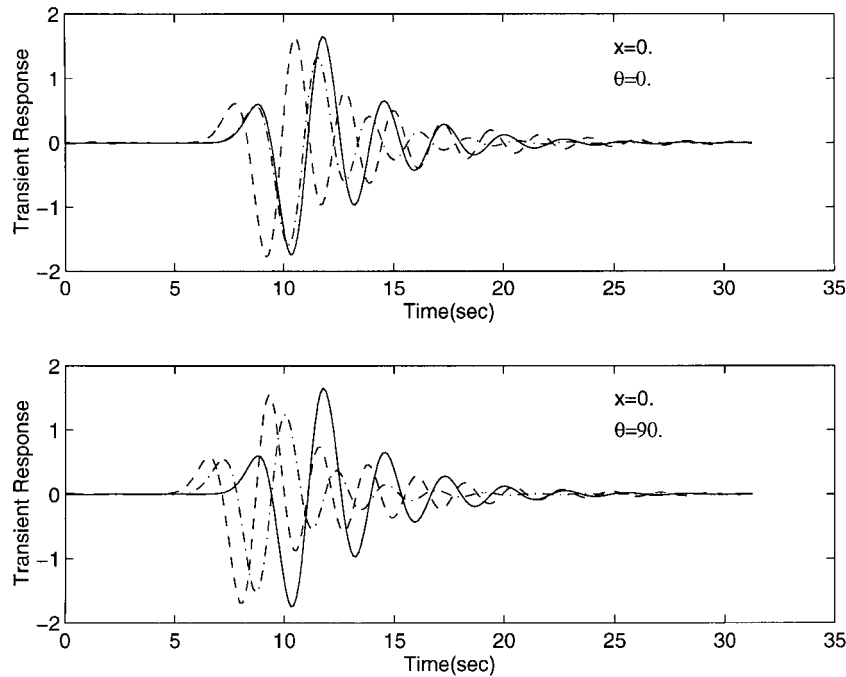


Figure 8. Comparison of transient surface response for semicircular basins: A (isotropic: solid), B (orthotropic: dash-dot), and C (orthotropic with higher impedance contrast $I_{1,2}^C > I_{1,2}^B$: dash) at location $(0,0,0)$ for a vertical (top) and grazing (bottom) incident SH-Ricker wave. The wavefront at $t=0$ is the plane passing through the point $(x_0, y_0, z_0) = (0,0,10)$ for a vertical incidence and $(x_0, y_0, z_0) = (-10,0,0)$ for a grazing incidence. The other parameters are the same as in Figure 7

Transient response

The transient response for each model is computed from the steady-state solution through the Fourier synthesis according to the procedure suggested by Eshraghi and Dravinski.¹⁴ The input signal is a plane SH-Ricker wavelet¹⁵ defined as

$$f(t) = \frac{\sqrt{\pi}}{2}(\tau - 0.5) \exp(-\tau), \quad \tau = [\pi(t - t_s)/t_p]^2 \quad (35)$$

where t_s corresponds to the peak amplitude in the time domain and t_p identifies the circular frequency $\omega_p = 2\pi/t_p$ which is associated with the maximum amplitude in the frequency domain. Throughout this section, the Ricker wavelet parameters are chosen to be $t_p = 4$ s and $t_s = 5$ s. Although the transient response calculations were done for three angles of incidence ($\theta_0 = 0^\circ, 45^\circ$, and 90°) the results are presented only for a vertical incidence. The transient response for the four models shown in Figure 7 gives the overall characteristics of the surface ground motion. More detailed comparison between the transient results for the four models can be made from Figures 8 and 9. Figure 8 displays the response at a single station ($x=0, z=0$) for three semicircular basins (models A, B, and C). Figure 9 compares the response at ($x=0, z=0$) for semicircular and semielliptical anisotropic models (B and B1). Based on these results, the following observations can be made about the transient response:

1. The presence of the basin may cause significant amplification of the surface motion.
2. While the peak amplitudes may be similar for all four models, the corresponding durations may vary considerably from one model to another. As expected, an increase in impedance contrast resulted in longer duration of surface motion.

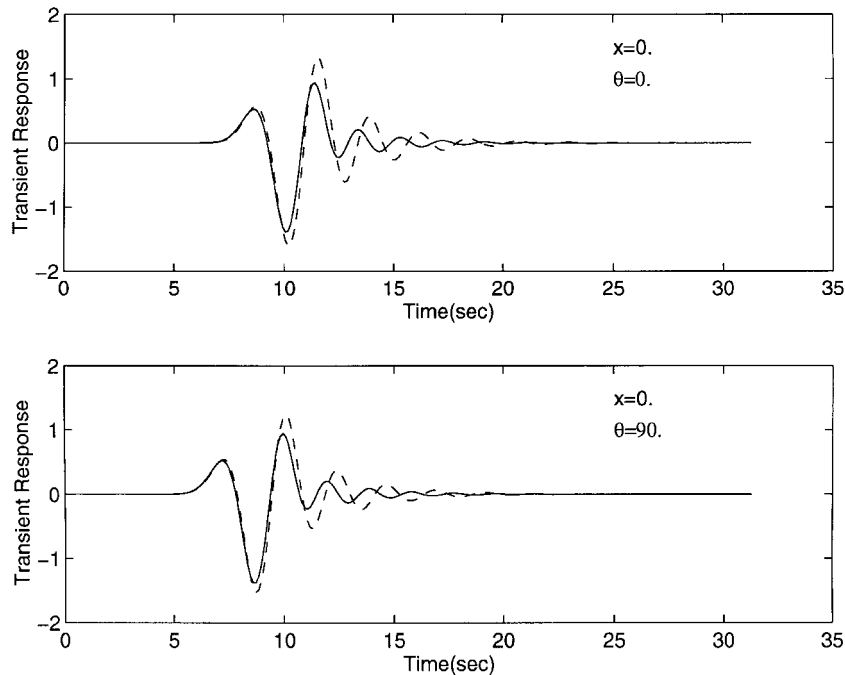


Figure 9. Comparison of transient surface response for a semicircular (model B: solid) and semielliptic (model B1: dash) basins at location $(0,0,0)$ for a vertical (top) and grazing (bottom) incident SH-wave. The wavefront at $t=0$ is the plane passing through the point $(x_0, y_0, z_0) = (0,0,10)$ for a vertical incidence and $(x_0, y_0, z_0) = (-10,0,0)$ for a grazing incidence. The other parameters are the same as in Figure 7

3. Decrease in valley depth produced reduction of the surface amplification.
4. Material anisotropy results in different arrival times for different models at various angles of incidence.

This concludes the transient analysis of the problem.

SUMMARY AND CONCLUSIONS

By using an indirect boundary integral equation method, scattering of SH-waves by an orthotropic sedimentary basin was investigated. Three different orthotropic models were compared with an isotropic one. Semicircular and semielliptical basins with different material properties were considered. Both steady-state and transient motions were obtained. The main results can be summarized as follows:

Surface response is found to be strongly dependent upon the nature of incident wave (frequency and angle of incidence), location of observation points, and material and geometry of the valley. The steady-state response of an orthotropic model may be very different from the corresponding isotropic one.

The fundamental resonant frequency of each model was obtained through spectral search method. It was shown that in comparison to the isotropic case material anisotropy changes the fundamental resonant frequency of the basin. While the resonant frequency is independent of the angle of incidence and the impedance contrast between the basin and the bedrock, it is strongly affected by the basin geometry.

The transient response of each model subjected to a plane SH-Ricker wavelet was obtained for different angles of incidence. The seismograms clearly demonstrate the role of the basin in the ground motion amplification. For cases considered here, larger impedance contrast produced longer duration of the response. Finally,

transient results show different arrival times at the surface of the half-space when comparing isotropic with anisotropic basins of the same geometry.

Overall, presented results demonstrate the importance of anisotropy in assessing surface ground motion atop sedimentary basins.

ACKNOWLEDGEMENTS

The support from All University Predoctoral Merit Fellowship at University of Southern California to one of the authors is greatly appreciated.

REFERENCES

1. D. E. Beskos, 'Boundary element method in dynamic analysis', *Appl. Mech. Rev.* **40**(1), 1–23 (1987).
2. M. Bouchon and O. Coutant, 'Calculation of synthetic seismograms in a laterally varying medium by the boundary element — discrete wavenumber method', *Bull. Seism. Soc. Am.* **84**, 1869–1881 (1994).
3. R. Rajapakse and D. Gross, 'Transient response of an orthotropic elastic medium with a cavity', *Wave Motion* **21**, 231–252 (1995).
4. Y.-G. Li, 'Seismic wave propagation in anisotropic media with applications to defining fractures in the Earth', *Ph.D. Thesis*, University of Southern California, 1988.
5. V. Babuska and M. Cara, *Seismic Anisotropy in the Earth*, Kluwer Academic Publishers, Dordrecht, MA, 1991.
6. A. H. Nayfeh, *Wave Propagation in Layered Anisotropic Media*, Elsevier, Amsterdam, 1995.
7. H. Karabulut and J. F. Ferguson, 'SH wave propagation by discrete wavenumber boundary integral modeling in transversely isotropic medium', *Bull. Seism. Soc. Am.* **86**(2), 524–529 (1996).
8. F. Ursell, 'On the exterior problems of acoustics', *Proc. Cambridge Philos. Soc.* **74**, 117–125 (1973).
9. M. Dravinski, 'Scattering of plane harmonic SH waves by dipping layers of arbitrary shape', *Bull. Seism. Soc. Am.* **73**, 1303–1319 (1983).
10. F. J. Sanchez-Sesma and F. Luzon, 'Seismic response of three-dimensional alluvial valleys for incident P, S, and Rayleigh waves', *Bull. Seism. Soc. Am.* **85**(1), 269–284 (1995).
11. A. Bjorck, *Numerical Methods for Least Squares Problems*, SIAM, Philadelphia, PA, 1996.
12. G. Ding and M. Dravinski, 'Scattering of SH waves in multilayered media with irregular interfaces', *Earthquake Engng. Struct. Dyn.* **25**, 1391–1404 (1996).
13. P. Y. Bard and M. Bouchon, 'The two-dimensional resonance of sediment-filled valleys', *Bull. Seism. Soc. Am.* **75**, 519–541 (1985).
14. H. Eshraghi and M. Dravinski, 'Transient scattering of elastic waves by dipping layers of arbitrary shape. Part 1. Antiplane strain model', *Earthquake Engng. Struct. Dyn.* **18**, 397–415 (1989).
15. N. Ricker, *Transient Waves in Visco-elastic Media*, Elsevier, Amsterdam, 1977.
16. M. D. Trifunac, 'Surface motion of a semi-cylindrical alluvial valley for incident plane SH waves', *Bull. Seism. Soc. Am.* **61**(6), 1755–1770 (1971).
17. T. Zhou and M. Dravinski, 'Resonance of sediment filled valleys and its prediction through an eigenvalue method', *Geophys. J. Int.* **117**, 749–762 (1994).